RSC Advances

PAPER

View Article Online
View Journal | View Issue

Check for updates

Cite this: *RSC Adv.*, 2025, **15**, 37109

Non-metallic SERS on MoO_x/AZO heterostructures: role of charge transfer and polarons

Trong Vo Huu, [ab] Nhi Nguyen Bich, [ab] Thanh Cu Duy,[ac] Tuan Dao Anh,[ab] Ke Nguyen Huu[ab] and Hung Le Vu Tuan *[ab]

Received 23rd July 2025
Accepted 25th September 2025

DOI: 10.1039/d5ra05314e

rsc.li/rsc-advances

In this study, a non-noble-metal SERS substrate based on MoO_x/Al-doped ZnO (AZO) heterostructures was successfully fabricated using a cost-effective DC magnetron sputtering method. The AZO thin film, optimized at a sputtering power of 45 W, provides a highly crystalline, textured surface, and optical characteristics that support both a chemical and electromagnetic enhancement mechanism. Upon deposition of a thin MoO_x layer for 7.5 minutes, the resulting heterostructure exhibits improved light absorption, enhanced defect-level emissions, and significant SERS activity. Spectroscopic analyses (UV-Vis, Raman, PL, and XPS) of the MoO_x/AZO heterostructures confirm the presence of oxygen vacancies and mixed-valence Mo^{5+}/Mo^{6+} species, indicative of small polaron formation. These polarons, along with interfacial energy alignment, enable efficient charge transfer from the SERS substrate to the analyte, supporting the chemical enhancement mechanism. Meanwhile, localized field enhancement at surface protrusions and junctions contributes to electromagnetic effects. The optimized MoO_x/AZO substrate achieved a detection limit as low as 10^{-7} M for Rhodamine 6G. This work underscores the critical impact of charge transfer and polaron-assisted processes in boosting Raman signals, highlighting the promise of oxide-based heterostructures for sensitive and scalable metal-free SERS applications.

1. Introduction

The development of Surface-Enhanced Raman Scattering (SERS) substrates is driven by the need to detect organic substances at low limits of detection (LOD) with high enhancement factors (EF). Conventional SERS platforms rely on noble metal nanoparticles, such as gold (Au), silver (Ag), and copper (Cu), which amplify Raman signals through the electromagnetic (EM) mechanism.[1] This enhancement arises from localized surface plasmon resonance (LSPR), generating intense electric fields at "hot spots" where interparticle distances are on the nanometer scale, yielding EFs from 10^5 to 10^8.[2] The chemical mechanism (CM) also plays a significant role by enabling chemical interactions between the analyte and the substrate, altering the polarizability of the probe molecule and promoting charge transfer (CT) at the molecule–substrate interface. According to Cong S. *et al.*, three main charge transfer pathways account for CM-based enhancements.[1] The first is ground-state charge transfer (μ_{GSCT}). In this pathway, signal enhancement by μ_{GSCT} is a non-resonant contribution characterized by chemisorption interactions between the molecule and the substrate in the ground state, without excitation. The polarizability in the metal-molecule complex can be altered through surface charge transfer to generate a larger intrinsic Raman scattering cross-section and fluctuations in the Raman spectral shape. The second mechanism is photon-induced charge transfer (μ_{PICT}), which is a wavelength-dependent process occurring when the energy of incident photons enables electron transfer between the metal and the molecule. This transfer direction either from metal to molecule or *vice versa* depends on the relative alignment of the metal's Fermi level and the molecule's highest occupied molecular orbital (HOMO) and lowest unoccupied molecular orbital (LUMO). Finally, resonance Raman scattering (RRS) occurs when the laser excitation frequency closely matches the molecule's electronic transition, leading to direct excitation from the HOMO to the LUMO. This effect is particularly pronounced in fluorescent molecules. Overall, the CM mechanism can contribute enhancement factors in the range of 10^2 to 10^6.[1] Thus, both EM and CM mechanisms complement each other in SERS enhancement and warrant continued investigation.

Besides charge transfer, the polaron effect also plays an important role in SERS. The concept of an electron interacting with a crystal lattice to create a self-trapping potential well was first proposed by Landau in 1933, leading to Solomon Pekar's formulation of the polaron in 1946.[2] By the 1950s, a distinction emerged between large polarons characterized by weak electron-phonon coupling, as described by Herbert Fröhlich and small polarons, which involve strong electron-phonon interactions and hopping transport mechanisms, as detailed

[a]University of Science, Ho Chi Minh City, Vietnam. E-mail: lvthung@hcmus.edu.vn
[b]Vietnam National University, Ho Chi Minh City, Vietnam
[c]National Central University, Taiwan

Open Access Article. Published on 07 October 2025. Downloaded on 2/24/2026 2:39:45 PM.
This article is licensed under a Creative Commons Attribution-NonCommercial 3.0 Unported Licence.

Open Access Article. Published on 07 October 2025. Downloaded on 2/24/2026 2:39:45 PM. This article is licensed under a Creative Commons Attribution-NonCommercial 3.0 Unported Licence.

by Theodore Holstein.[3] This concept has found renewed importance in explaining the high efficiency of modern perovskite solar cells through a "polaron screening" mechanism that prolongs carrier lifetimes. In parallel, the field of SERS is shifting focus from noble metals to semiconductor substrates, where the CM becomes pivotal.[4–6] Consequently, polarons are now being investigated for their potential role in this mechanism.

However, to the best of our knowledge, no prior studies have explicitly demonstrated the contribution of polarons to SERS enhancement. This work aims to provide direct evidence of such a contribution by investigating the role of polarons in the SERS chemical enhancement mechanism on semiconductor substrates. This study proposes that polarons are a key contributor to the SERS signal, offering a physical basis that may inform the design of SERS devices with engineered polaron properties.

Traditionally, SERS substrates have been fabricated using noble metal nanoparticles (*e.g.*, Au, Ag, Pt) to leverage their surface plasmon resonance effect. However, these noble metal-based SERS substrates suffer from several drawbacks, including high cost, variable stability due to oxidation upon prolonged air exposure, and signal dependency on 'hotspot' distributions.[7] Consequently, a recent trend in SERS research is the investigation and development of semiconductor-based substrates as a promising alternative to their noble metal counterparts. In recent studies, notable examples of semiconductor-based materials include ZnO, TiO_2, MoO_x, WO_x and Cu_2O.[8,9] These materials offer unique physicochemical properties, such as oxygen vacancies, tunable band structures, stability, and reduced photothermal effects that enable alternative signal amplification mechanisms beyond traditional plasmonics. For instance, Lili Yang *et al.* demonstrated that hydrated TiO_2 substrates could achieved a limit of detection (LOD) as low as 10^{-7} M for Rhodamine 6G (R6G) after a 3 hours hydration treatment.[10] Similarly, Xudong Zheng *et al.* synthesized a WO_x substrate *via* heat treatment, creating oxygen-deficient structures capable of detecting R6G over a concentration range from 10^{-1} M to 10^{-7} M, and methylene blue down to 10^{-8} M.[8,11] MoO_x-based materials have also attracted attention due to their inherent oxygen vacancy characteristics, yielding R6G detection limits between 10^{-7} and 10^{-8} M.[12–14] Recent studies have also demonstrated that constructing semiconductor heterojunctions can significantly boost SERS sensitivity. By aligning energy bands at the interface, heterostructures facilitate efficient CT pathways and synergistically combine EM and CM effects. For example, Anxin Zhang *et al.* fabricated a nano-arrayed Cu_2S@MoS_2 heterostructure that successfully detected methylene blue at concentrations as low as 10^{-8} M.[15] Collectively, these findings underscore the growing potential of non-metallic SERS substrates. Semiconductor-based systems, in particular, offer an exciting and versatile platform for further development in high-sensitivity molecular detection.

Among these semiconductors, zinc oxide (ZnO) is a widely studied semiconductor material with applications spanning solar cells, photocatalysis, surface-enhanced Raman scattering (SERS), and light-emitting devices (LEDs), among others. It is well known for its wide bandgap (~3.3 eV) and distinctive physical, chemical, and optoelectronic properties.[16] One of the key advantages of ZnO lies in its versatility of synthesis methods, which allow the formation of a variety of nanostructures such as nanorods, nanobelts, nanocombs, nanorings, and nanosprings to significantly increase the effective surface area.[17,18] For SERS applications, ZnO functions as a high-refractive-index semiconductor, which enhances light trapping and consequently boosts SERS enhancement.[16] Its nanostructured forms not only contribute to a larger active surface area but also enable the integration of noble metal nanoparticles, promoting the formation of electromagnetic "hot spots" and amplifying the Raman signal *via* the electromagnetic (EM) mechanism. Furthermore, doping ZnO with aluminum (resulting in Al-doped ZnO, or AZO) transforms it into an n-type semiconductor with increased charge carrier concentration. This enhancement can facilitate more efficient CT interactions between the substrate and analyte, further boosting the SERS signal *via* the CM. Various AZO morphologies have also been shown to produce localized electric field enhancements, somewhat analogous to those in noble metal substrates, albeit typically of lower intensity. Taken together, these properties make AZO a highly promising candidate for the fabrication of efficient and cost-effective SERS substrates.

Similarity, molybdenum trioxide (MoO_3) is also gaining significant attention due to the unique characteristics of its oxygen deficiencies, enabling its development in many applications. For instance, its high work function of ~6.6 eV allows it to be used as a hole transport layer in c-Si solar cells.[6,19] In photocatalysis, oxygen-deficient MoO_x provides active sites that function as electron traps, thereby enhancing catalytic efficiency.[20,21] In the field of SERS, MoO_x is also proving to be a potential candidate under investigation. A comprehensive review by Chenjie Gu highlights MoO_x and its various synthesis strategies for SERS applications. Furthermore, studies on TiO_2@MoO_x fabricated by the hydrothermal method have also been shown to enhance SERS, achieving a detection capability for R6G at a concentration of 10^{-8} M.[22] Work by Songyang Xie's group on MoO_x/WO_x heterolayers featuring MoO_x nanobelts embedded with WO_x nanoparticles also reported detection of R6G at the same concentration.[23] Ongoing research continues to explore the unique properties of MoO_x, particularly those arising from its oxygen deficiencies, making it a highly active and promising area of study in SERS and beyond.

Research on MoO_x/AZO heterostructures for SERS remains limited, with only a few studies exploring their applications in fields such as photocatalysis and solar cells. In the present study, we aim to address this gap by fabricating a novel SERS substrate composed of an AZO thin film and a thin MoO_x overlayer using a DC magnetron sputtering technique. Here, AZO is deposited as a continuous thin film, serving multiple roles: it acts as a charge transfer medium to promote the CM mechanism, provides a structural foundation for the uniform deposition of a MoO_x overlayer, and offers active sites for analyte adsorption. Meanwhile, the MoO_x overlayer, deposited as a dispersed thin layer on the AZO surface, contributes additional CT channels, defect states, and small polarons, alongside

© 2025 The Author(s). Published by the Royal Society of Chemistry

Open Access Article. Published on 07 October 2025. Downloaded on 2/24/2026 2:39:45 PM. This article is licensed under a Creative Commons Attribution-NonCommercial 3.0 Unported Licence.

localized field enhancement akin to LSPR. The engineered energy level mismatch at the MoO_x/AZO interface is expected to facilitate interfacial CT, thus driving CM processes. Through systematic optimization of sputtering power and deposition times, we demonstrate that this heterostructure effectively leverages both EM and CM mechanisms, particularly CT and polaron-assisted processes, to achieve high SERS sensitivity. To the best of our knowledge, this study represents one of the first demonstrations of MoO_x/AZO heterostructures as efficient, entirely metal-free SERS platforms, highlighting their promise for low-cost and sensitive molecular detection.

2. Experimental and method

In this study, SERS substrates were fabricated entirely on glass slides using the DC magnetron sputtering technique (Leybold Univex-450). The AZO film was deposited from the 3-inch aluminum-doped zinc oxide (AZO) target with 2 at% Al concentration, prepared from ZnO (Merck, 99.9%) and Al_2O_3 (Merck, 99.5%) powders. While the MoO_x layer was formed using a high-purity molybdenum (Mo) target (99.95%, ACI Alloys). Prior to deposition, the glass substrates were cleaned with a 15% NaOH solution, followed by sequential sonication in methanol, acetone, and deionized water. Subsequently, an AZO layer was deposited onto the cleaned substrates *via* sputtering. Finally, the as-deposited samples were annealed in air at 500 °C for 6 hours.

AZO thin films of varying characteristics were then fabricated by adjusting the DC sputtering power. The overall experimental procedure is summarized in the schematic diagram presented in Fig. 1.

AZO thin films were deposited at sputtering powers of 15, 30, 45, and 60 W, and are referred to as AZ_15, AZ_30, AZ_45, and AZ_60, respectively. For comparison, a pure ZnO film sputtered at 15 W was prepared as a reference and designated Z_15. The detailed deposition parameters are summarized in Table 1.

Next, the AZ_45 sample, which exhibited the optimal structure and surface morphology (see Fig. 5 and 6), was selected as the optimized AZO substrate. A thin MoO_x layer was then deposited onto this substrate *via* reactive sputtering to form the MoO_x/AZO heterostructure SERS substrate.

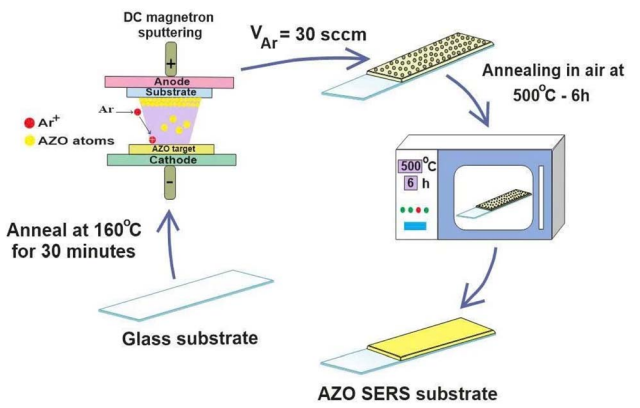

Fig. 1 Schematic illustration of the fabrication process for AZO-based SERS substrates using the DC magnetron sputtering technique.

Table 1 Deposition parameters for AZO thin films fabricated on glass substrates by DC sputtering

Sample	Time (minutes)	Power (W)
AZ_15	90	15
AZ_30		30
AZ_45		45
AZ_60		60
Z_15 (ZnO)		15

The sputtering time was systematically varied from 2.5 to 12.5 minutes at a constant power of 15 W, resulting in samples labeled MA_2.5, MA_5, MA_7.5, MA_10, and MA_12.5, as illustrated in Fig. 2.

Notably, because both the AZO thin film and the thin MoO_x layer were fabricated using the same DC sputtering technique, the experimental procedure is relatively straightforward and enables precise control over key deposition parameters—including thickness, morphology, and composition—which are critical for optimizing SERS performance.

To compare the fabricated SERS substrate in this study with a noble-metal-based counterpart, Ag nanoparticle (AgNP) substrates were synthesized *via* a microwave-assisted method followed by centrifugation, using the optimized parameters reported previously.[24] Briefly, 0.5 mL of $AgNO_3$ (50 mM), 0.5 mL of sodium citrate solution (44 mM), and 99 mL of deionized water were mixed and subjected to microwave irradiation at 60 W for 15 min. The resulting colloidal solution (1000 μL) was centrifuged in an Eppendorf tube to collect AgNPs at the bottom. After removing 980 μL of the supernatant, 20 μL of concentrated AgNPs was retained. For the comparative experiment, this AgNP suspension was mixed with 50 μL of R6G solution (10^{-5} M) and drop-cast on a glass to assess the Raman signal enhancement capability.

The crystal structure of the MoO_x/AZO films was characterized using X-ray diffraction (XRD) using a Bruker AXS D8 Advance diffractometer with Cu-K_α radiation (λ = 1.541 Å). Surface morphology and cross-sectional features were examined by field-emission scanning electron microscopy (FE-SEM; Hitachi S4800). The optical properties of the films were analyzed using UV-visible absorption spectroscopy (Halo RB-10) and photoluminescence (PL) spectroscopy (Cary Eclipse MY2246CG04) with an excitation wavelength of 250 nm. X-ray photoelectron spectroscopy (XPS, Thermo VG-Scientific Sigma Probe, equipped with an Al-K_α X-ray source, 1486.6 eV) was also performed to investigate the elemental composition and chemical states.

The SERS performance was evaluated by measuring the signal enhancement of the R6G analyte using a Horiba XploRa PLUS Raman spectrometer equipped with a 1200 grooves per mm grating. Raman measurements were carried out with a 532 nm laser excitation source operating at 1.5 mW, focused onto a ~2 μm diameter spot on the sample surface. The spectrometer was calibrated before measurements using the

Open Access Article. Published on 07 October 2025. Downloaded on 2/24/2026 2:39:45 PM.
This article is licensed under a Creative Commons Attribution-NonCommercial 3.0 Unported Licence.

Fig. 2 Schematic illustration of the fabrication process for MoO_x nanoparticle-decorated AZO thin-film SERS substrates *via* DC magnetron sputtering.

characteristic silicon peak at 520 cm^{-1}. Spectra were acquired with an integration time of 2 seconds and 3 accumulations, with the laser power attenuated to 10% of its maximum output.

3. Results

3.1. Characteristics of AZO thin films

In this section, based on the characterization results, the AZO film exhibiting the most favorable properties for Raman signal enhancement was selected for subsequent SERS studies.

Fig. 3a displays the UV-Vis spectra for the AZO samples, which were sputtered at powers of 15, 30, 45, and 60 W, along with a ZnO sample sputtered at 15 W for comparison. The spectra show that the absorption edges of all AZO samples exhibit a slight blueshifted relative to ZnO sample. Furthermore, as the sputtering power increases, the absorption edge shifts further toward the ultraviolet region. These observations are consistent with previous reports from other research groups on AZO films.[25,26]

Based on the absorption spectroscopy results, Tauc plots were constructed to determine the bandgap energy (E_g) of the samples, as shown in Fig. 3b. The ZnO sample exhibits an E_g of 3.23 eV, while the E_g values for the AZO samples increase with sputtering power: 3.33 eV for AZ_15, 3.40 eV for AZ_30, 3.43 eV for AZ_45, and 3.49 eV for AZ_60.

The observed increase in E_g for the AZO samples compared to pure ZnO originates from the substitution of Zn^{2+} ions with Al^{3+} ions, which introduces additional free electrons and enhances the n-type semiconductor behavior. The electrons generated by this substitution occupy the lowest available energy states at the bottom of the conduct band (CB), effectively filling them. As a result, electron excitation from the valence band (VB) requires a higher energy to reach the next available unoccupied states in the CB. This shift in the absorption edge leads to an apparent widening of the bandgap, commonly known as the Moss–Burstein effect. This effect has been previously reported and confirmed in related literature on AZO.[25,27,28]

Moreover, the absorbance in both the UV and visible regions is higher for samples AZ_30, AZ_45, and AZ_60 compared to AZ_15. This indicates that the film thickness increases with higher sputtering power, resulting in enhanced light absorption.

Based on the UV-Vis spectra, the AZ_30, AZ_45, and AZ_60 samples exhibit strong absorption in the visible region, making them well-suited for excitation with a 532 nm laser in SERS

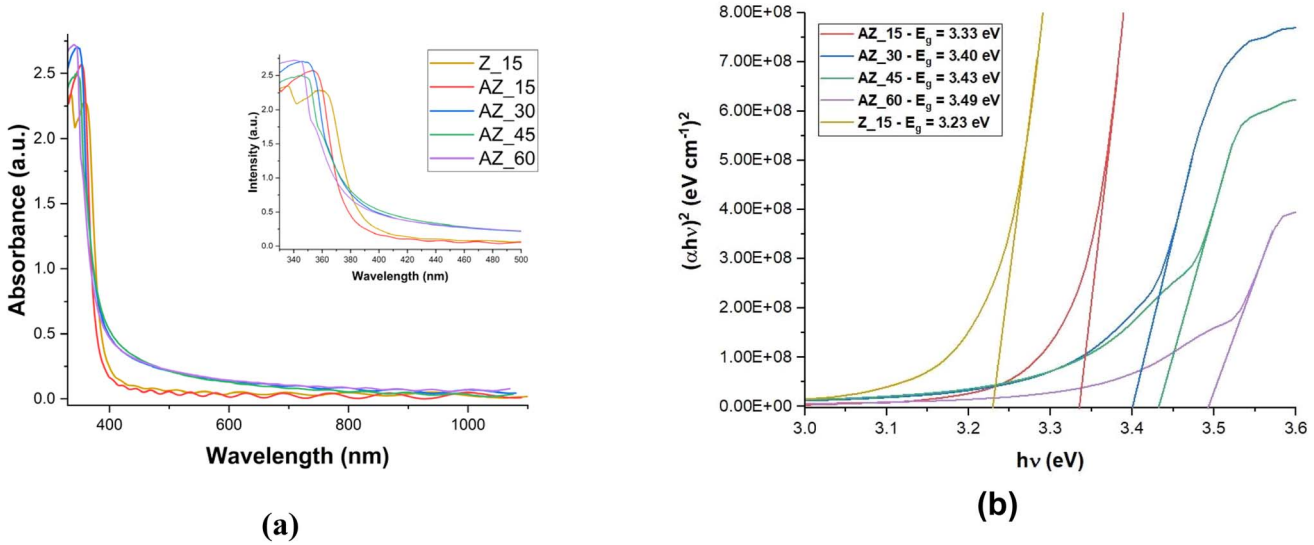

Fig. 3 (a) UV-Vis absorption spectra of ZnO and AZO thin films deposited at different sputtering power. (b) Estimated optical band gap (E_g) values of ZnO and AZO films as a function of sputtering power.

© 2025 The Author(s). Published by the Royal Society of Chemistry

Open Access Article. Published on 07 October 2025. Downloaded on 2/24/2026 2:39:45 PM. This article is licensed under a Creative Commons Attribution-NonCommercial 3.0 Unported Licence.

applications. Additionally, the significant variation in the optical bandgap (E_g) among these samples offers a broader selection of SERS substrates for analyzing target molecules with different energy levels.

To further investigate the structural characteristics of the fabricated samples, XRD and Raman spectroscopy measurements were performed.

Fig. 4a reveals clear structural differences between the pure ZnO and AZO samples. For the pure ZnO sample (Z_15), the XRD pattern exhibits diffraction peaks at $2\theta = 31.80°$, 34.40°, and 36.25°, corresponding to the (100), (002), and (101) planes, respectively, as indexed by JCPDS No. 36-1451.[29] The ZnO film shows preferential growth along the (100) plane, which is typically favored under low surface energy and limited adatom mobility. In contrast, the incorporation of Al dopants in AZO modifies the lattice parameters and surface energy. Combined with the higher energy conditions of the sputtering process, this promotes preferential orientation along the (002) plane. Moreover, the diffraction peaks of the AZO samples are slightly shifted toward lower 2θ angles, indicating lattice expansion due to oxygen vacancies introduced during fabrication.

Ideally, the characteristic Raman modes of ZnO are observed at 102 cm^{-1} (E_2(low)), 379 cm^{-1} (A_1(TO)), 410 cm^{-1} (E_1(TO)), 439 cm^{-1} (E_2(high)), 574 cm^{-1} (A_1(LO)), and 591 cm^{-1} (E_1(LO)), corresponding to different optical phonon vibrations.[30,31] The Raman spectra of the investigated samples are presented in Fig. 4b. To guide the eye, vertical dashed lines mark the positions of the primary Raman peaks discussed, specifically at 276 cm^{-1}, 435 cm^{-1}, and 578 cm^{-1}. In its spectrum, the Z_15 sample clearly exhibits a dominant peak at 435 cm^{-1}, which is assigned to the E_2(high) mode, characteristic of the hexagonal wurtzite structure. Additionally, a peak is observed at 578 cm^{-1}, the pronounced intensity of which is typically attributed to structural defects, such as oxygen vacancies and zinc interstitials, within the ZnO lattice.[32–34]

Under the identical sputtering conditions, all AZO samples exhibit a prominent and sharp peak at 435 cm^{-1}, also corresponding to the E_2(high) mode and indicating excellent crystallization with a hexagonal wurtzite structure. The appearance of the 578 cm^{-1} peak in these samples also confirms the presence of structural defects. Furthermore, a mode at 276 cm^{-1}, corresponding to the Raman-activated B_1(low) vibration, is observed in all AZO samples. The emergence of this otherwise forbidden mode is attributed to the substitution of Zn^{2+} by Al^{3+} ions in the lattice, which induces local symmetry distortions. This finding is in good agreement with previous reports on Al-doped ZnO materials.[24,26,30,31]

XRD and Raman analyses reveal that the AZ_45 sample exhibits the highest crystallinity, along with defect structures that are conducive to CT mechanisms in SERS.

The Fröhlich model describes the interaction between an electron and longitudinal optical (LO) phonons *via* a dimensionless coupling constant α, given by the eqn (1) below:[35]

$$\alpha = \frac{e^2}{\hbar} = \left(\frac{m^*}{2\omega_{LO}}\right)^{0.5}\left(\frac{1}{\varepsilon_\infty} - \frac{1}{\varepsilon_0}\right) \quad (1)$$

The parameters in this equation are defined in the Table 2 below:

Using the provided data in Table 2, eqn (1) yields a coupling constant of $\alpha = 1.04$. A value of $\alpha \approx 1$ indicates the presence of large polarons in the AZO, which are weakly coupled to the lattice and remain delocalized as they move through the material.[2] These delocalized electrons can participate in charge transfer processes at the interface between the AZO substrate and organic molecules, and their mobility helps homogenize the SERS signal across the substrate. However, for the R6G analyte, this charge transfer occurs with low probability due to the significant energy level mismatch.

When comparing the SEM images of ZnO and AZO films prepared under identical conditions (Fig. 5a and b), the ZnO film displays a smooth, compact surface morphology with indistinct grain boundaries, indicative of low porosity and high surface density. In contrast, the AZO films exhibit increased

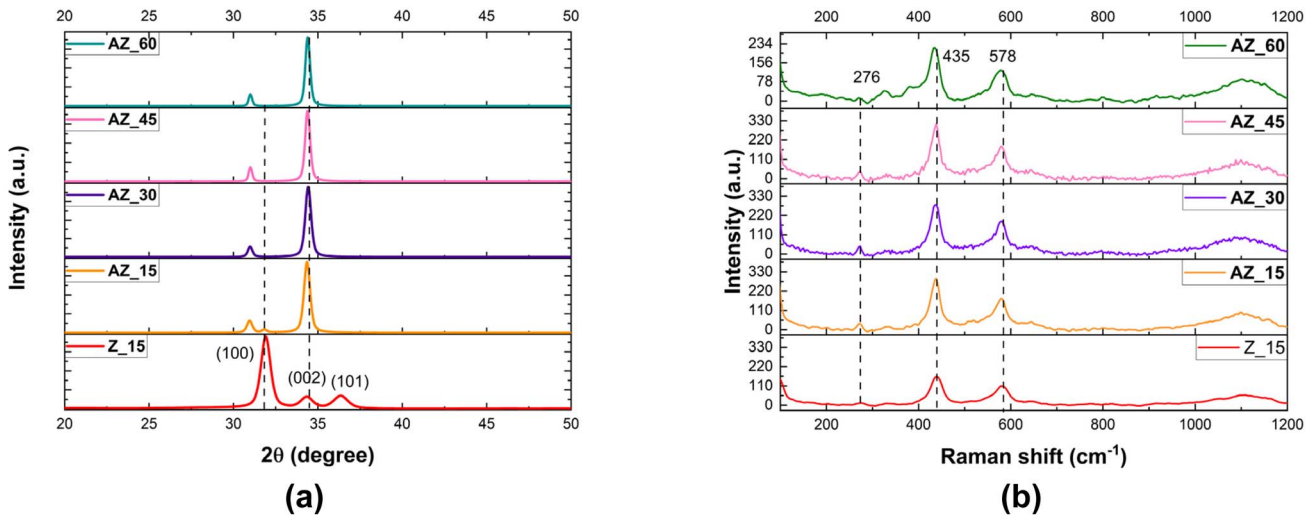

Fig. 4 (a) XRD pattern and (b) Raman spectra of Z_15, AZ_15, AZ_30, AZ_45, AZ_60 samples.

Open Access Article. Published on 07 October 2025. Downloaded on 2/24/2026 2:39:45 PM. This article is licensed under a Creative Commons Attribution-NonCommercial 3.0 Unported Licence.

Table 2 The parameters of Fröhlich model[35]

Symbol	Description	Given value	Unit
e	Electron charge	1.602×10^{-19}	Coulomb
$\hbar$	Reduced Planck constant	6.582×10^{-16}	eV s
m^*	Carrier effective mass	$0.27\ m_0$	kg
m_0	Free electron rest mass	9.11×10^{-31}	kg
ω_{LO}	LO phonon frequency	578 cm^{-1} (from Raman spectrum in Fig. 4b) = 0.0715 eV	eV
ε_∞	High-frequency dielectric constant	3.2	—
ε_0	Static dielectric constant	8.6	—

surface roughness, suggesting that aluminum incorporation markedly influences the microstructural evolution and growth behavior of the films.

SEM images of the AZO films (Fig. 5b–e) illustrate clear morphological evolution corresponding to increased film grain as the sputtering power increases. At 15 W (AZ_15), the surface consists of relatively large, irregularly shaped grains interspersed with numerous voids, characteristic of an initial, non-uniform growth stage. With increasing power to 30 W (AZ_30), grain size becomes larger and the structure more orderly, indicating a transition toward improved crystallinity. A pronounced change is observed at 45 W (AZ_45), where grains adopt vertically oriented, well-defined polygonal shapes with sharp edges, reflecting enhanced crystallization and sustained nucleation. This results in a rough yet cohesive surface, which is advantageous for subsequent MoO_x deposition due to improved interfacial adhesion. However, at 60 W (AZ_60), continued grain growth leads to substantial particle agglomeration and overlap, forming dense clusters that effectively reduce the available surface area. This may adversely impact SERS performance by limiting hotspots and light matter interaction sites.

Based on these observations, the AZ_45 film is identified as the optimal substrate. It combines high crystallinity, well-developed grains, and a relatively uniform morphology with enhanced absorption in the visible range. Consequently, AZ_45 was selected as the base layer for MoO_x deposition. Under these sputtering conditions, the AZO surface exhibits a nanostructured architecture that facilitates efficient light matter interactions and promotes charge transfer processes both essential for achieving superior SERS enhancement.

To conduct a preliminary evaluation of the enhancement capabilities of the fabricated ZnO and AZO substrates, R6G analyte at a concentration of 10^{-4} M was used. For each SERS substrate, 50 μL of the aqueous R6G solution was drop-casted, followed by Raman spectral measurements. The results are presented in Fig. 6. The Raman spectrum of R6G exhibits several characteristic peaks. The prominent peaks at 1360, 1510, and 1650 cm^{-1} are assigned to aromatic C–C stretching vibrations. The C–H in-plane bending modes are observed at 1125 cm^{-1} and 1180 cm^{-1}, while the C–H out-of-plane bending mode appears at 771 cm^{-1}. Furthermore, the peaks at 1311 cm^{-1} and 1575 cm^{-1} are attributed to N–H in-plane bending vibrations. Finally, the peak at 609 cm^{-1} corresponds to the C–C–C ring in-plane bending mode.[36]

The results indicate that the sputtered ZnO and AZO samples exhibit relatively weak Raman enhancement for R6G. Although the Raman signals of R6G on AZO substrates are consistently stronger than those on ZnO, the characteristic Raman peaks of R6G remain poorly defined and are not well resolved from the background. This limited enhancement is primarily attributed

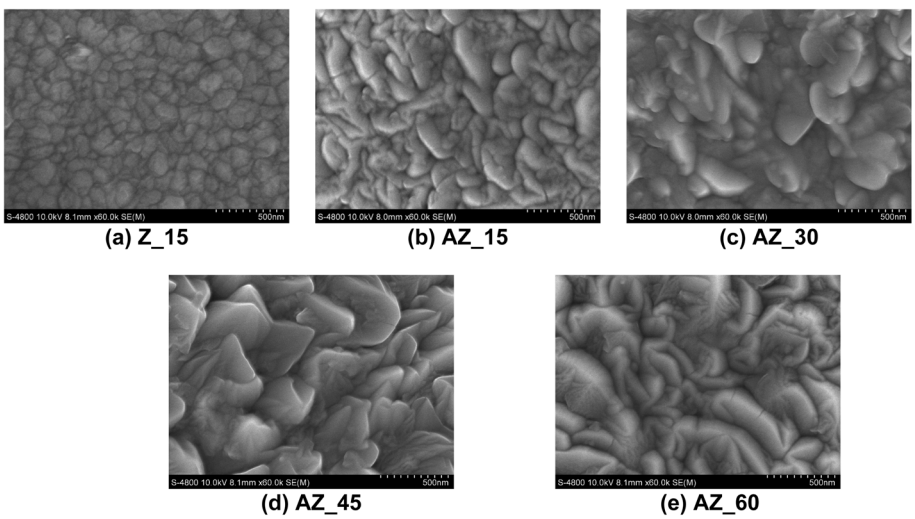

Fig. 5 SEM image surface of (a) Z_15; (b) AZ_15; (c) AZ_30; (d) AZ_60; (e) AZ_90 samples.

© 2025 The Author(s). Published by the Royal Society of Chemistry

Open Access Article. Published on 07 October 2025. Downloaded on 2/24/2026 2:39:45 PM.
This article is licensed under a Creative Commons Attribution-NonCommercial 3.0 Unported Licence.

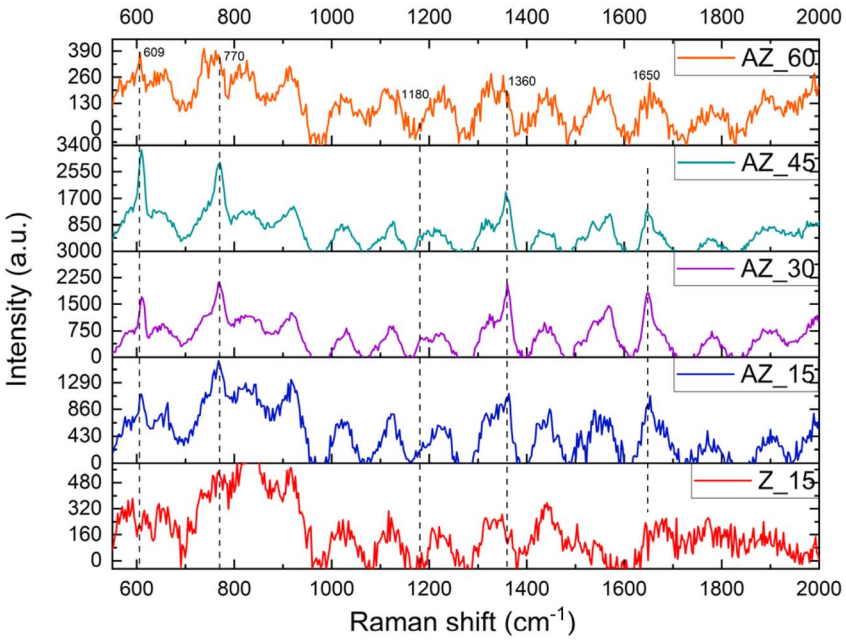

Fig. 6 Raman spectra of R6G at a concentration of 10^{-4} M on Z_15; AZ_15; AZ_30; AZ_45; AZ_60 substrates.

to the use of semiconductor based SERS substrates, where the signal amplification mainly occurs *via* the CM mechanism. However, a minor contribution from the EM mechanism may also exist, as the electrons introduced by Al doping, together with the sharp edges and corners on the AZO surface, can generate localized electric fields that enhance the Raman signal. Among the tested samples, AZ_45 exhibits relatively clearer and more distinguishable R6G Raman peaks, which aligns well with the superior structural and morphological properties discussed earlier.

3.2. Characteristics of MoO_x/AZO heterostructures

The MoO_x/AZO SERS substrates (MA_2.5, MA_5, MA_7.5, MA_10, and MA_12), whose fabrication process is illustrated in Fig. 2, were characterized as follows.

The UV-Vis absorption spectra of the MA_2.5, MA_5, MA_7.5, MA_10, and MA_12.5 samples exhibit distinct variations in absorption intensity (Fig. 7a), indicating that increased MoO_x loading enhances photon absorption capability. All MA samples display an absorption shoulder or a broad absorption band in the near-UV region (approximately 300–380 nm).

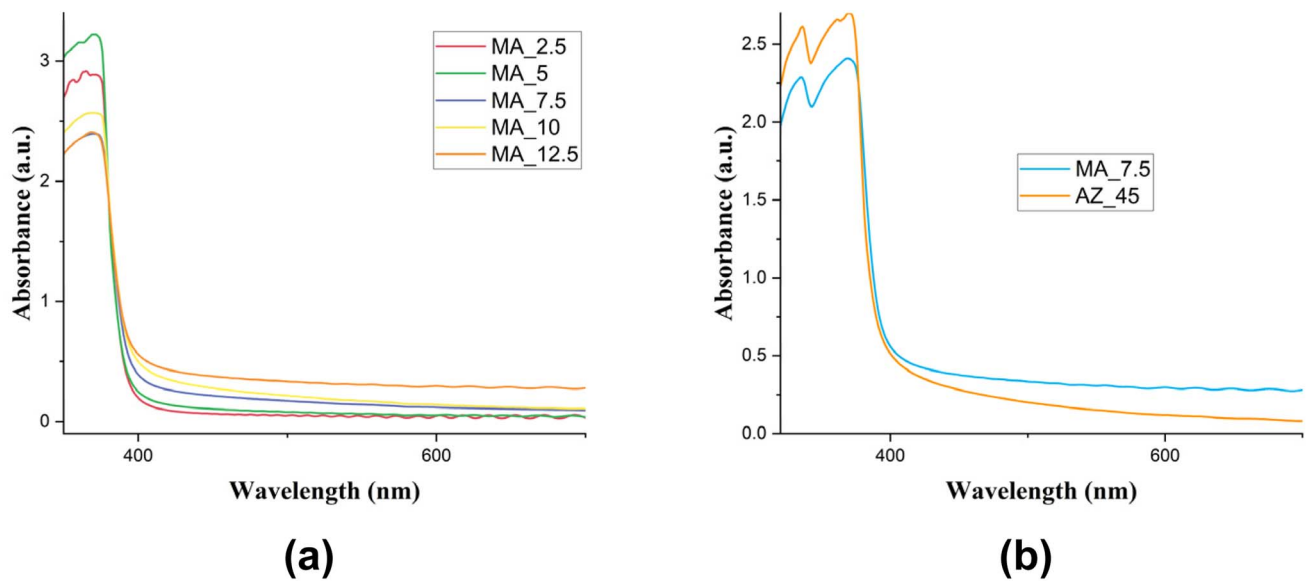

Fig. 7 (a) UV-Vis absorption spectra of MA_2.5, MA_5, MA_7.5, MA_10, and MA_12.5 samples. (b) The comparison of UV-Vis spectra between AZ_45 and MA_7.5.

Open Access Article. Published on 07 October 2025. Downloaded on 2/24/2026 2:39:45 PM.
This article is licensed under a Creative Commons Attribution-NonCommercial 3.0 Unported Licence.

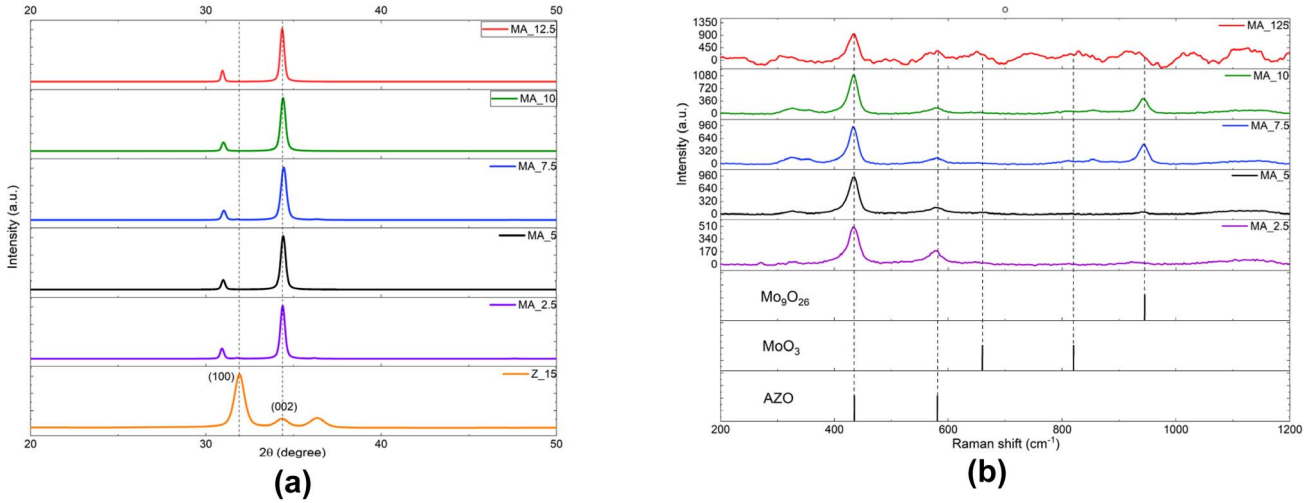

Fig. 8 (a) The XRD pattern and (b) the Raman spectra of MA_2.5, MA_5, MA_7.5, MA_10 and MA_12.5 samples.

When comparing MA_7.5 with AZ_45 in Fig. 7b, it is clear that the presence of the MoO_x layer on the AZO surface significantly enhances optical absorption across visible regions approximately 400–700 nm. This observation suggests that the MoO_x layer serves as the dominant contributor to light absorption in the heterostructure.

The XRD pattern in Fig. 8a shows that the structure of the MoO_x/AZO heterostructures remains unchanged compared to that of the single AZO films (Fig. 4a), indicating that the deposited MoO_x layer is thin and induces minimal structural changes in the underlying heterostructure.[29] The Raman spectra in Fig. 8b reveal that, in addition to the characteristic peaks of AZO, the MA_2.5, MA_5, MA_7.5, and MA_10 samples also exhibit a Raman peak at 946 cm^{-1}, corresponding to the presence of Mo_9O_{26}.[12,37] In contrast, the MA_12.5 sample, with a thicker MoO_x layer, shows a peak at 820 cm^{-1}, characteristic of the more stable MoO_3 phase.[38]

To investigate the surface morphology of the MoO_x/AZO heterostructures, SEM imaging was performed on the samples (Fig. 9). Compared to the pure AZ_45 sample shown in Fig. 5, the additional sputtering of MoO_x resulted in the formation of thin MoO_x layers within the crevices of the AZO structure. As the sputtering time increased, these layers became more prominent and gradually formed a continuous film over the AZO surface, particularly in the MA_10 and MA_12.5 samples.

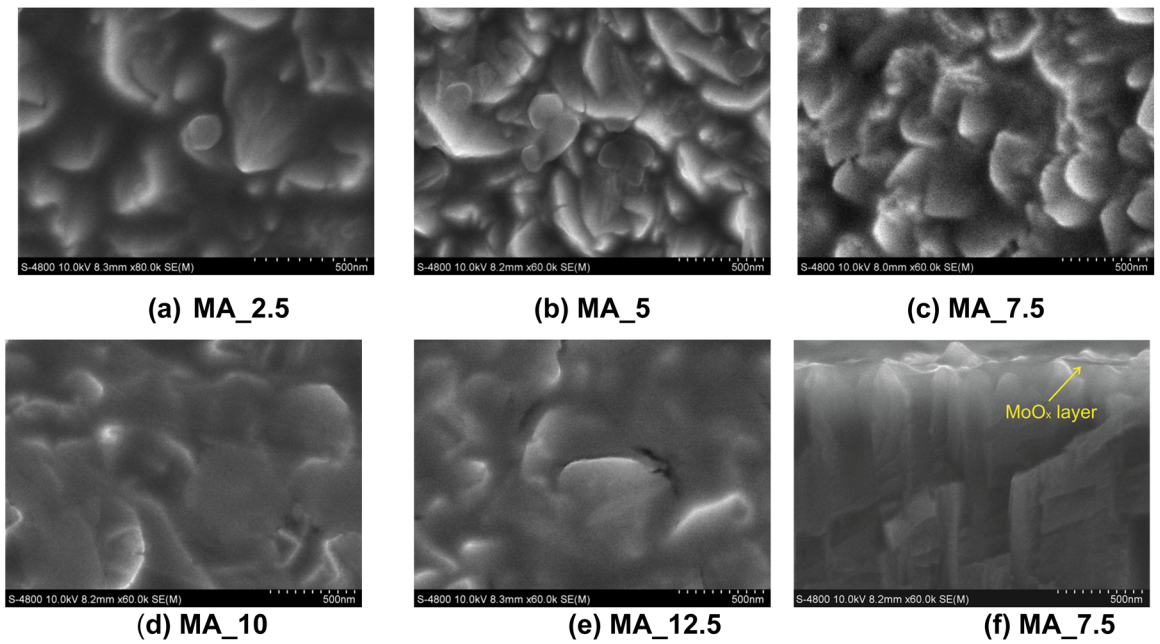

Fig. 9 (a)–(e) SEM images of the MA_2.5, MA_5, MA_7.5, MA_10, and MA_12.5 samples. (f) The cross-sectional SEM image of the MA_7.5 sample.

© 2025 The Author(s). Published by the Royal Society of Chemistry

Open Access Article. Published on 07 October 2025. Downloaded on 2/24/2026 2:39:45 PM. This article is licensed under a Creative Commons Attribution-NonCommercial 3.0 Unported Licence.

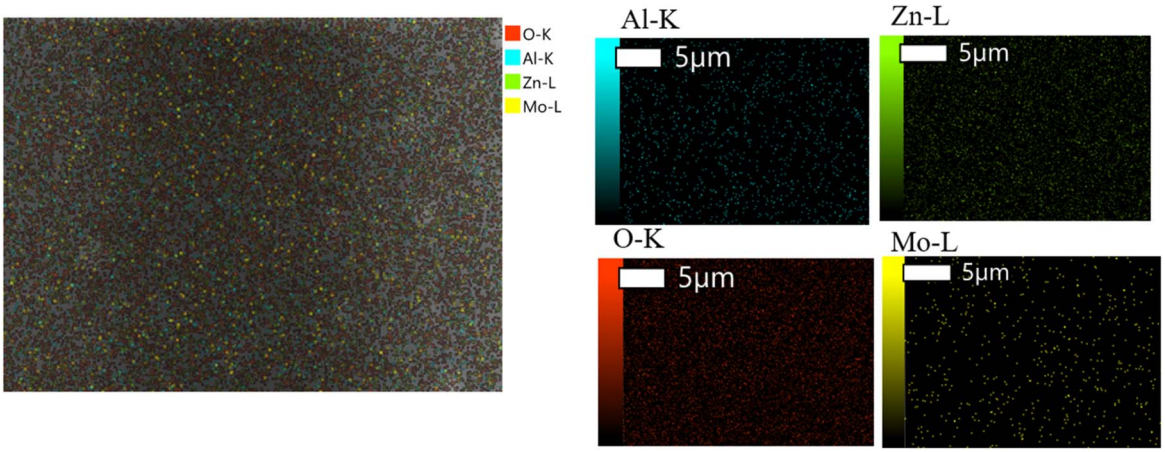

Fig. 10 EDS mapping image and individual elemental EDX analysis of the MA_7.5 sample.

The MA_7.5 sample has a MoO_x thin layer uniformly coated on the AZO surface, while not being too thick to completely fill the porous gaps on the ZnO surface. As a result, the effective surface area of the substrate remains high, ensuring its usefulness for SERS enhancement. As the sputtering time increased further, the MA_10 and MA_12.5 samples exhibited a tendency for the MoO_x layer to agglomerate into larger clusters. The surface appeared denser, with fewer gaps and reduced nanoscale roughness compared to MA_7.5.

The cross-section SEM image of the MA_7.5 sample in Fig. 9f shows a thin MoO_x layer uniformly coating the AZO structure.

Therefore, the MA_7.5 sample exhibits significant potential for the development of SERS substrates. The uniform elemental distribution of the MA_7.5 sample is observed through the EDS spectra in Fig. 10.

Based on the EDS mapping image of the MA_7.5 sample in Fig. 10, it is evident that oxygen (O) and zinc (Zn) are the elements with wide distribution and high percentages. In contrast, aluminum (Al) and molybdenum (Mo), which serve as dopants or additional components, are present in lower percentages. The presence of the Mo element confirms the formation of a MoO_x layer on the AZO substrate, and its distribution is quite uniform across the analyzed area (Table 3).

The photoluminescence (PL) spectrum of pure ZnO (Fig. 11a) exhibits two prominent emission regions: one in the ultraviolet range (380–400 nm), corresponding to near-band-edge (NBE) exciton recombination, and another in the visible range (400–800 nm), attributed to defect-level emissions (DLE). The DLE is generally associated with intrinsic defects, including oxygen vacancies (V_O), zinc vacancies (V_{Zn}), oxygen interstitials (O_i), and zinc interstitials (Zn_i).[39] In AZO thin films, shifts in the binding energy of Zn have been reported, arising from energy transfer interactions between Zn^{2+} and Al^{3+} ions.[40] However, in the PL spectrum of MA_7.5 sample in Fig. 11b, no emission is observed in the NBE region from ZnO. The emissions are predominantly confined to the DLE region. This is likely because the MoO_x layer coated onto the AZO substrate can induce charge transfer effects at the MoO_x/AZO interface. When forming a semiconductor heterostructure, the MoO_x layer can act as an electron-trapping medium, capturing electrons from the AZO layer and thereby suppressing radiative recombination at the band edge. Consequently, this leads to a significant attenuation or even complete quenching of the NBE emission from ZnO.

Table 3 Elemental composition of the MoO_x/AZO sample

Element	Wt%	At%
O	62.97 ± 0.79	89.36 ± 1.02
Zn	27.98 ± 0.85	8.83 ± 0.27
Al	2.20 ± 0.21	1.69 ± 0.16
Mo	0.55 ± 0.24	0.12 ± 0.05

The peaks observed in the visible DLE region of MA_7.5 sample can be categorized into four types: violet, blue, yellow, and red-near infrared (NIR). These emissions result from the recombination of electron–hole pairs through various defect related energy states within the band gap. The violet emission (~435 nm, 2.85 eV) is typically attributed to transitions involving localized defect states rather than extended defect band.[41] These states are often linked to zinc interstitials (Zn_i) or shallow oxygen vacancies (V_O), which introduce energy levels close to the conduction band minimum. The blue emission (~467 nm, 2.66 eV) arises from transitions from the conduction band to zinc vacancy (V_{Zn}) levels, suggesting an increased concentration of zinc vacancies.[40] The yellow emission (~578 nm, 2.15 eV) is generally ascribed to transitions from the conduction band to oxygen interstitial (O_i) levels.[40] The red-NIR emission (~733 nm) is uncommon in pristine ZnO and is likely associated with new defect or trap states introduced at the MoO_x/AZO interface. This emission may also be influenced by the potential plasmonic activity of MoO_x.[40,41] The appearance of this 733 nm peak suggests that the interaction at the MoO_x/AZO heterojunction creates new energy levels within the band gap.[40] These levels act as recombination centers for electron–hole pairs, causing near-infrared emission.

© 2025 The Author(s). Published by the Royal Society of Chemistry

Open Access Article. Published on 07 October 2025. Downloaded on 2/24/2026 2:39:45 PM. This article is licensed under a Creative Commons Attribution-NonCommercial 3.0 Unported Licence.

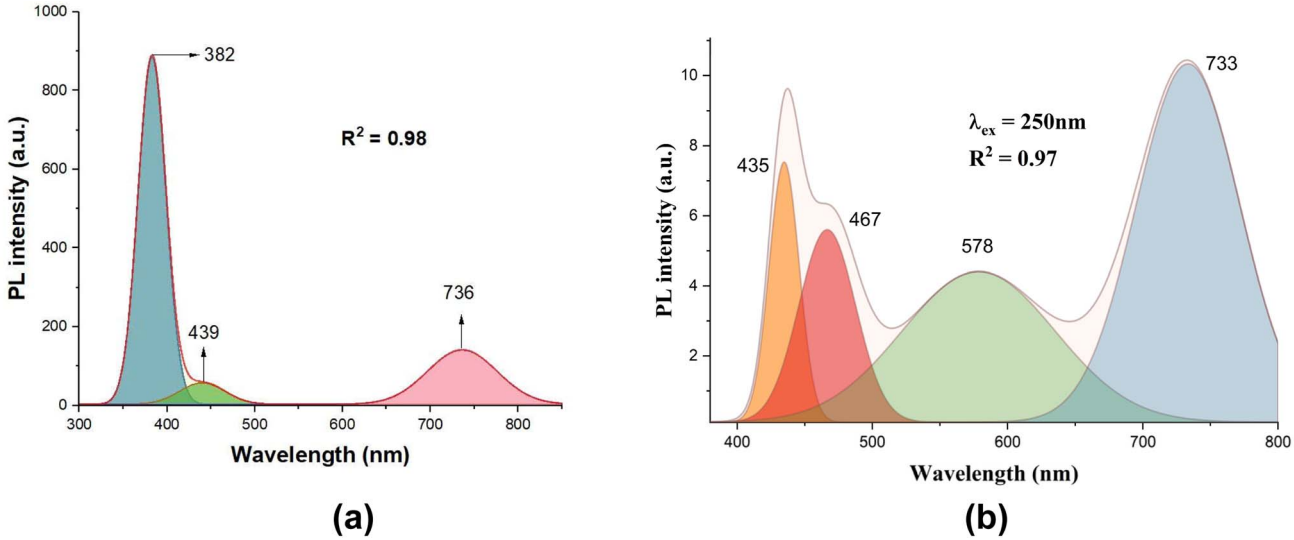

Fig. 11 Gaussian deconvolution PL spectrum of (a) AZ_45 and (b) MA_7.5 sample.

The PL spectrum of the MA_7.5 sample indicates the presence of various structural defects, particularly oxygen related and other deep-level defects. These defects act as radiative recombination centers and may enhance the performance of the material as a SERS substrate by promoting the CM mechanism in the SERS process.

X-ray Photoelectron Spectroscopy (XPS) was employed to analyze the chemical composition and bonding states of the elements (Zn, O, Al, and Mo) in the fabricated MA_7.5 sample. The corresponding XPS spectra are shown in Fig. 12. As shown in Fig. 12a, the high-resolution XPS spectrum of Zn 2p exhibits two characteristic peaks at 1022.4 eV (Zn $2p_{3/2}$) and 1045.5 eV (Zn $2p_{1/2}$). The energy separation of 23.1 eV between these peaks confirms that zinc is present exclusively in the Zn^{2+} oxidation state.[42,43]

Fig. 12b shows the O 1s XPS spectrum. Deconvolution of this spectrum using Gaussian functions reveals two distinct peaks at binding energies of 531.6 eV and 528.8 eV.[44] The peak at 531.6 eV is assigned to lattice oxygen in Zn–O bonds of the ZnO crystal lattice and in Mo–O bonds. The peak at 528.8 eV indicates the presence of oxygen vacancies within the SERS substrate, arising from both the ZnO and MoO_x components. These oxygen deficiencies are expected to significantly influence the optical properties of the sample.

Fig. 12c shows a characteristic peak for the Al 2p core level at a binding energy of 74.7 eV.[40] This value corresponds to the Al^{3+} oxidation state, confirming the successful incorporation of aluminum into the ZnO lattice *via* Al–O bonds rather than existing as metallic clusters.

To determine the electronic states of MoO_{3-x}, the Mo 3d XPS spectrum was analyzed, as shown in Fig. 12d. Peaks at 233.3 eV and 236.27 eV are assigned to Mo^{6+} $3d_{5/2}$ and Mo^{6+} $3d_{3/2}$, respectively, while those at 231.1 eV and 235.0 eV correspond to Mo^{5+} $3d_{5/2}$ and Mo^{5+} $3d_{3/2}$.[42,43] No peaks associated with Mo^{4+} were detected, indicating the absence of this oxidation state. The coexistence of Mo^{5+} and Mo^{6+} confirms the non-stoichiometric nature of MoO_{3-x}. Based on the Mo^{5+}/Mo^{6+} area ratio, the value of x was estimated to be 0.15, corresponding to a stoichiometry of $MoO_{2.85}$. This result aligns well with the Raman spectral features attributed to Mo_9O_{26}, as presented in Fig. 8b. Oxygen vacancies typically form at grain boundaries or structural defect sites on the substrate.[39] Such non-stoichiometry introduces additional electronic states within the band gap, enhancing the electrical conductivity of the material.[45] Moreover, Greiner *et al.* reported that increased defect concentrations in MoO_3 lead to changes in the work function and band structure, thereby facilitating stronger interactions with analytes.[46]

Furthermore, the previously discussed PL spectrum for the MA_7.5 sample exhibited strong emission peaks in the visible and near-infrared regions, which were attributed to deep-level defects, particularly oxygen vacancies. These XPS results are fully consistent with and reinforce the findings from the PL spectroscopy.

Therefore, the combined structural and surface analyses indicate that the MA_7.5 sample exhibits strong potential for SERS enhancement.

3.3. Evaluation of R6G analyte on MoO_x/AZO SERS substrates

To evaluate the Raman enhancement capability of the MoO_x/AZO substrates, the MA_7.5 sample was selected for detailed analysis. As an initial step, 50 μL of Rhodamine 6G (R6G) solution was drop-cast onto the MA_2.5, MA_5, MA_7.5, MA_10, and MA_12.5 samples. The corresponding Raman spectra obtained from these samples are presented in Fig. 13a.

As shown in Fig. 13a, the Raman spectra indicate that the MA_7.5 sample exhibits the strongest Raman enhancement among all tested substrates. After sputtering MoO_x onto the AZO layer, the background signal decreases, and the characteristic Raman peaks of R6G become more distinct. In contrast, other samples either present poorly defined peaks or exhibit elevated background signals that obscure the Raman features of R6G.

© 2025 The Author(s). Published by the Royal Society of Chemistry

Open Access Article. Published on 07 October 2025. Downloaded on 2/24/2026 2:39:45 PM. This article is licensed under a Creative Commons Attribution-NonCommercial 3.0 Unported Licence.

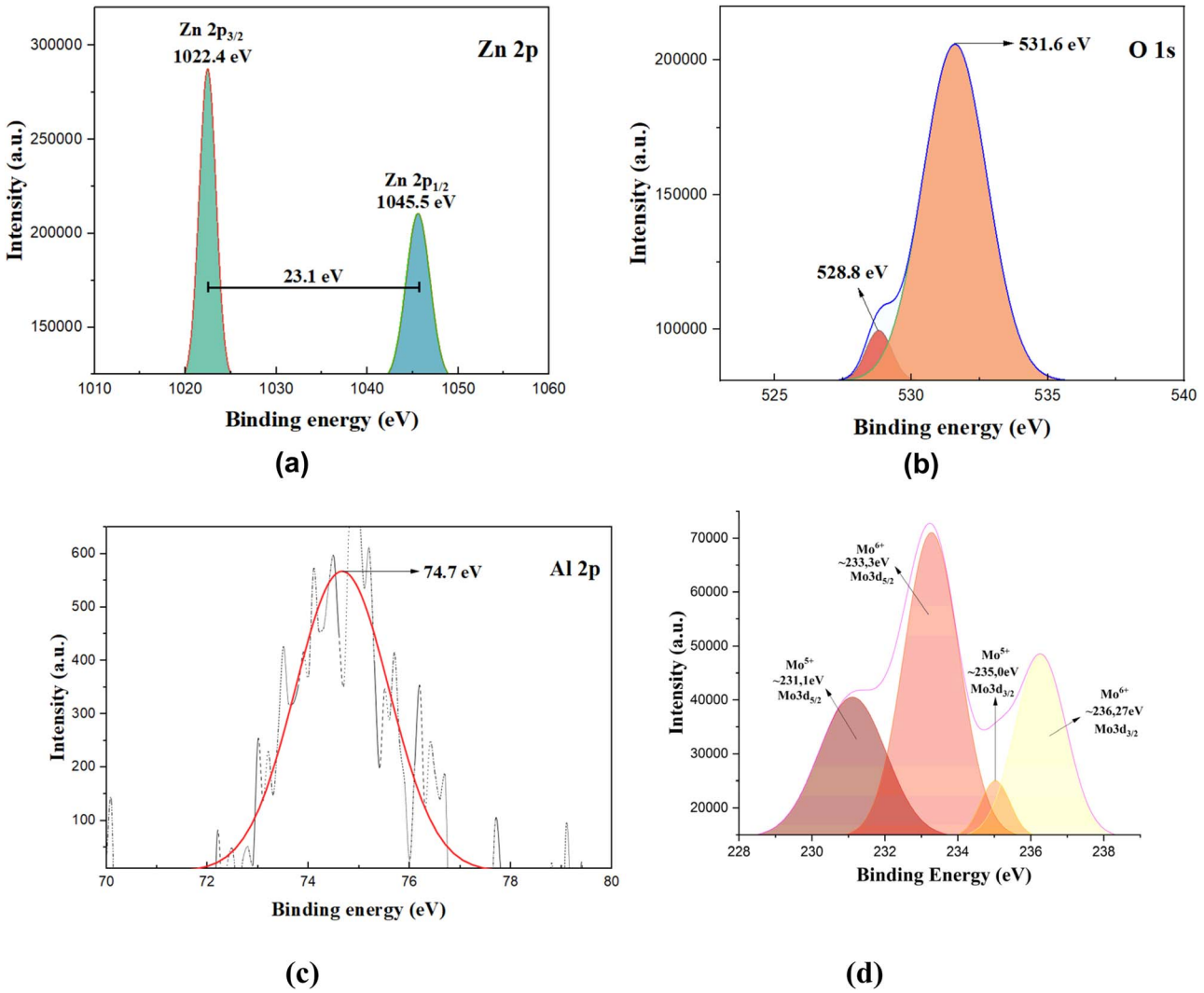

Fig. 12 High-resolution XPS spectra of the MA_7.5 sample: (a) Zn 2p spectrum; (b) O 1s spectrum; (c) Al 2p spectrum; (d) Mo 3d spectrum.

As mention above for the MA_10 and MA_12.5 samples, the longer MoO_x sputtering time, which significantly reduces the Raman enhancement. This suggests that an excessively thick MoO_x film may hinder the formation of localized electric field hotspots essential for the EM mechanism. Moreover, when MoO_x forms a continuous thick layer, R6G molecules tend to adsorb on its surface without direct contact with the underlying AZO, thereby limiting the CT from AZO to R6G. Consequently, this further diminishes the overall Raman signal intensity.

The reproducibility of the fabricated MoO_x/AZO heterostructure was investigated. Three independent samples were fabricated using the same parameters as for sample MA_7.5 and were subsequently tested as SERS substrates for detecting 10^{-6} M R6G. As shown in Fig. 13b, the Raman spectra from the three samples were highly consistent. The average intensity of the characteristic peak at 609 cm^{-1} was 2105 a.u., yielding a relative standard deviation (RSD) of only 2.1%. These results confirm the excellent reproducibility and uniformity of the proposed fabrication method.

To further evaluate the performance of the MA_7.5 SERS substrate, its limit of detection (LOD) was assessed using R6G solutions with concentrations ranging from 10^{-3} M to 10^{-7} M. As shown in Fig. 13c, even at a concentration as low as 10^{-7} M, several characteristic Raman peaks of R6G are still discernible, although with reduced intensity. At concentrations below this level, the Raman signals are expected to fall below the detection threshold, rendering the characteristic peaks undetectable.

Based on these results, Fig. 13d presents a linear relationship between the Raman intensity and the logarithm of the R6G concentration, exhibiting an excellent correlation coefficient (R^2 = 0.993). This strong linearity underscores the reliable sensitivity of the MA_7.5 substrate across a wide range of analyte concentrations.

To evaluate the signal uniformity of the substrate, Raman spectra were collected from six randomly selected positions on a sample using a 10^{-6} M R6G solution. The resulting spectra are presented in Fig. 13e. The characteristic peaks of the R6G analyte were clearly observed at all measured locations. The mean intensity of the 609 cm^{-1} peak was 2236 a.u., with

Open Access Article. Published on 07 October 2025. Downloaded on 2/24/2026 2:39:45 PM.
This article is licensed under a Creative Commons Attribution-NonCommercial 3.0 Unported Licence.

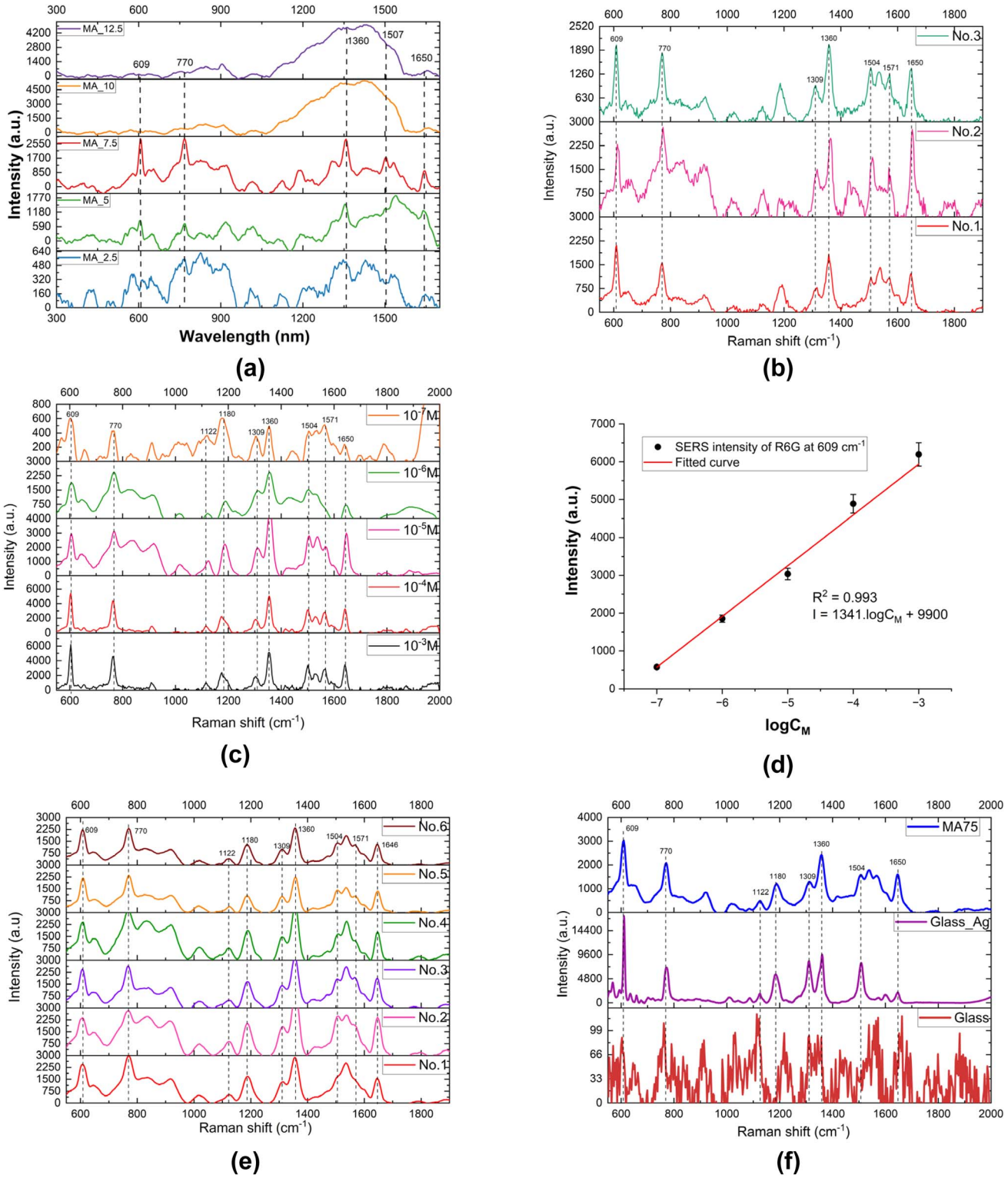

Fig. 13 (a) Raman spectra of 10^{-6} M R6G on MA_2.5, MA_5, MA_7.5, MA_10, and MA_12.5 substrates; (b) reproducibility of MA_7.5 SERS substrates tested with R6G (10^{-6} M); (c) Raman spectra of R6G at various concentrations (from 10^{-3} M to 10^{-7} M) on the MA_7.5 substrate; (d) the linear relationship between the SERS intensity of the Rhodamine 6G (R6G) peak at 609 cm^{-1} and the logarithm of its molar concentration. (e) Stability of the MA_7.5 SERS substrate evaluated by six successive measurements of R6G (10^{-6} M) on the same sample. (f) Raman spectra of R6G (10^{-5} M) on glass, glass–Ag, and MA_7.5 substrates.

© 2025 The Author(s). Published by the Royal Society of Chemistry

Open Access Article. Published on 07 October 2025. Downloaded on 2/24/2026 2:39:45 PM. This article is licensed under a Creative Commons Attribution-NonCommercial 3.0 Unported Licence.

a relative standard deviation (RSD) of 3.6%, indicating that the substrate possesses excellent signal uniformity.

To compare with other substrates, the SERS signals of 10^{-5} M R6G were measured, as shown in Fig. 13f. For the bare glass substrate, the R6G signal was extremely noisy, and its characteristic vibrational peaks were not distinguishable. Conversely, both the substrate with silver nanoparticles (fabricated by the microwave and centrifugation methods, as described in Section 2) and the MoO_x/AZO substrate produced clear Raman signals. The Raman enhancement from the noble metal nanoparticles is dominated by the EM, resulting in an intensity about five times stronger than the MoO_x/AZO semiconductor substrate. Nevertheless, owing to their superior stability and lower cost, semiconductor-based SERS substrates are an emerging trend aimed at replacing those based on noble metals.

3.4. SERS enhancement mechanism of the MoO_x/AZO substrate

Electromagnetic enhancement mechanism. In the MoO_x/AZO heterostructure, the EM enhancement primarily arises from the AZO layer, a conductive semiconductor oxide that inherently contains free electrons. Additionally, at specific surface sites of both MoO_x and AZO such as sharp corners, edges, or nanostructures with high curvature a local amplification of the electromagnetic field can occur, a phenomenon commonly known as the lightning rod effect.[47]

When subjected to an external electric field, such as incident light, the free electrons particularly those localized at these field-enhancing sites can undergo collective oscillations, giving rise to LSPR-like effects in AZO and MoO_x. Although the intensity of LSPR in semiconductor materials is generally weaker and red-shifted (often appearing in the infrared region) compared to that in noble metals like gold or silver, its contribution remains significant. This ability of AZO and MoO_x to support LSPR underscores their potential in plasmon-enhanced applications, including SERS, where they can facilitate electromagnetic field enhancement despite being non-metallic.

Chemical enhancement mechanism. The contribution of MoO_x through the CM mechanism is equally significant. In MoO_x, interactions between electrons often arising from oxygen vacancies and the crystal lattice lead to the formation of quasiparticles known as polarons.[48,49] Conduction *via* polaron hopping typically dominates over conventional band-to-band conduction due to its localized nature. A key consequence of this mechanism is the emergence of intermediate energy states within the band gap, which facilitate CT between the substrate and adsorbed analyte molecules. Furthermore, oxygen vacancies in MoO_x are generally concentrated near the surface, increasing the number of active sites for interaction with analytes. The localized character of polarons enhances their coupling with adsorbed organic species, thereby amplifying the CM contribution to the overall SERS signal.

The UV-Vis spectrum of the MA_7.5 sample was processed using the envelope fitting method to extract the underlying absorbance as a function of energy (Fig. 14a). According to the Holstein model, materials prone to small polaron formation are expected to display a characteristic optical absorption band in the NIR-visible region. This band arises from the photo-induced transition of an electron from its self-trapped polaron state to a neighboring site.[45,49,50] Accordingly, an absorption peak attributable to small polarons is anticipated in the UV-Vis spectrum of the material.

As mentioned in Section 3.1, the polaron in the ZnO crystal lattice is classified as a large polaron and is described by the Fröhlich model. In contrast, the existence of small polarons in the structure of MoO_x has been confirmed in the presence of oxygen vacancies. Consequently, to investigate the emergence of small polarons within the MoO_x structure, the Holstein model is employed instead of the Fröhlich model. In the Fröhlich model, although electrons interact with the crystal lattice, this interaction is relatively weak, allowing them to move quite freely through the lattice. This weak coupling is evidenced by the high electrical conductivity observed in AZO films. Conversely, in MoO_x, electrons interact very strongly with the crystal lattice, creating self-trapped states localized within a narrow region between two ions. As a result, electrons cannot move freely but instead migrate *via* a "hopping" mechanism.[51] This behavior is a characteristic feature of transition metal oxides (TMOs).

In their studies on small polarons based on the Holstein model, Austin and Mott proposed a model for the absorption coefficient. Specifically, the optical absorption coefficient can be expressed by eqn (2).[50,52,53]

$$\alpha_p(h\nu) = \frac{A_p}{h\nu}\exp\left(-\frac{(h\nu - 2E_p)^2}{8E_pE_{op}}\right) \quad (2)$$

with A_p as the polaron pre-exponential factor, E_p as the polaron binding energy, and E_{op} as the broadening energy.

To determine the position of this absorption band, the spectrum was fitted with an eqn (2), as illustrated in Fig. 14b. The fit shows excellent agreement ($R^2 = 0.9790$), revealing a peak centered at $E_p = 0.714$ eV.

To confirm that this absorption originates from small polarons, the dimensionless electron-phonon coupling constant (γ) was evaluated.[54] For MoO_x, prominent optical phonon modes was identified at 810 cm^{-1}, as shown in Raman spectra (Fig. 14c).[49] Using eqn (3), the calculated γ values for these modes are 7.38. Since $\gamma \gg 1$, this indicates a strong electron-phonon interaction, consistent with reported values for small polarons in transition metal oxides.[53] Accordingly, these results confirm the presence of small polarons in the fabricated thin MoO_x thin film.

$$\gamma = \frac{E_p}{\hbar\omega_o} \quad (3)$$

In summary, the MoO_x/AZO heterostructure offers several advantages for SERS enhancement. First, the large polaron characteristics of AZO facilitate efficient electron transfer to the MoO_x layer, thereby increasing the surface electron density available for interactions with analyte molecules. Second, the small polaron nature of MoO_x introduces mid-gap energy states

Open Access Article. Published on 07 October 2025. Downloaded on 2/24/2026 2:39:45 PM.
This article is licensed under a Creative Commons Attribution-NonCommercial 3.0 Unported Licence.

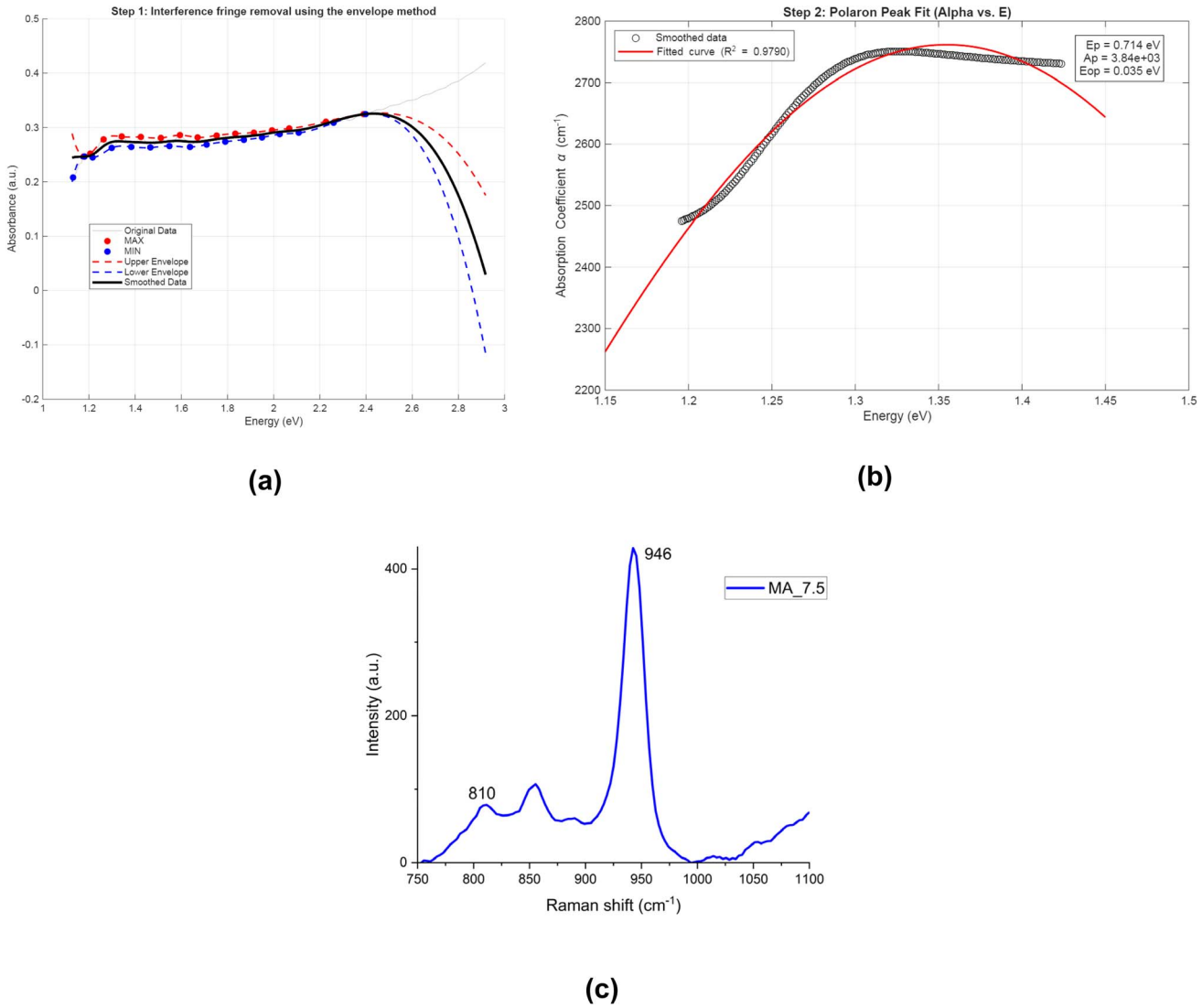

Fig. 14 (a) Interference fringe removal using envelope method. (b) Fit polaron peak using Gaussian according to Holstein model. (c) Raman spectra of MA_7.5 ranging from 750 cm^{-1} to 1100 cm^{-1}.

that serve as reactive sites, elevating the local density of states (LDOS) and promoting the charge-transfer process. This results in a more pronounced chemical enhancement compared to pristine AZO. Thus, the MoO_x/AZO heterojunction exploits a synergistic "transfer and trap" mechanism to achieve superior SERS performance.

Within this heterostructure, the difference in Fermi levels drives electron transfer from AZO to MoO_x, consequently increasing the polaron population at the interface. Based on the above discussions, a CT mechanism is proposed, as illustrated in Fig. 15.

The CT mechanism is widely proposed and accepted in studies concerning SERS. For CT to occur, two possible electron transition pathways have been proposed in the research by John Lombardi and co-workers, as follows: (1) from the valence band (VB) of the semiconductor material to LUMO of the analyte, and (2) from the HOMO of the analyte to the conduction band (CB) of the material.[55–57]

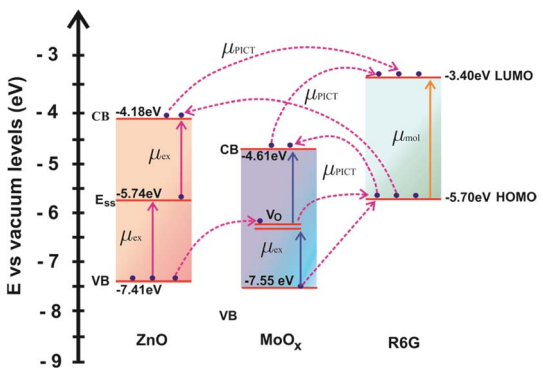

Fig. 15 Schematic diagram of CT between R6G and the MoO_x/AZO SERS substrate.

© 2025 The Author(s). Published by the Royal Society of Chemistry

Open Access Article. Published on 07 October 2025. Downloaded on 2/24/2026 2:39:45 PM. This article is licensed under a Creative Commons Attribution-NonCommercial 3.0 Unported Licence.

Using a 532 nm laser excitation (E_{ex} = 2.33 eV), the CT processes based on the proposed models are illustrated in Fig. 15. First, electrons in the valence band (VB) of MoO_x are photoexcited by the laser and acquire sufficient energy to transition to oxygen vacancy states (V_O). From these V_O levels, the electrons can readily transfer to the LUMO level of R6G. A second pathway involves photoexcitation of electrons from the VB of ZnO. A small fraction of these electrons can transition to surface defect states (E_{ss}) and then proceed to the conduction band (CB) of ZnO. From the CB, they may further transfer to the LUMO of R6G. However, electrons at the E_{ss} level are susceptible to trapping and exhibit low mobility, making their contribution to small signal enhancement. An additional pathway involves interfacial excitation at the MoO_x/AZO junction. In this mechanism, electrons are excited from the ZnO VB, transition through the V_O states of MoO_x, and ultimately reach the LUMO level of R6G.

As previously noted, the hopping-type CT mechanism enabled by MoO_x likely offers more effective Raman enhancement than conventional band-to-band transitions.

4. Conclusion

In this study, MoO_x/AZO SERS substrates were successfully fabricated using the DC magnetron sputtering method to enhance the Raman signal of the R6G analyte. By optimizing the AZO sputtering power, the best SERS performance was achieved at 45 W, resulting in an AZO film with favorable structural and optical characteristics. For the MoO_x layer sputtered for 7.5 minutes, Raman analysis confirmed the presence of the Mo_9O_{26} phase. The oxygen deficiency in MoO_x plays a crucial role in the formation of small polarons, which facilitate CT processes. The combination of AZO and MoO_x highlights the synergistic potential of this heterostructure for SERS applications. Specifically, the creation of a sharp-textured AZO surface followed by the deposition of MoO_x enables enhancement *via* both electromagnetic and chemical mechanisms. Besides, the research also points out experimental evidence for the existence of small polarons in the MoO_x structure with a binding polaron energy of $E_p = 0.714$ eV, which contributes to the enhancement of SERS *via* the CM mechanism. This approach achieved a limit of detection (LOD) of 10^{-7} M, demonstrating the promising performance of the MoO_x/AZO system as a SERS substrate.

Author contributions

Trong Vo Huu: investigation, measure, formal analysis, writing – original draft & editing. Nhi Nguyen Bich: synthesize, measure, analyze. Thanh Cu Duy: measure. Tuan Anh Dao: measure. Ke Nguyen Huu: review. Hung Le Vu Tuan: conceptualization, investigation, review & editing, supervision.

Conflicts of interest

There are no conflicts to declare.

Data availability

All data underlying the results are available as part of the article, and no additional source data are required.

Acknowledgements

This work was supported by Vietnam National University Ho Chi Minh City under grant number VL2024-18-03/HD-KHCN.

References

1 S. Cong, X. Liu, Y. Jiang, W. Zhang and Z. Zhao, *Innovation*, 2020, **1**, 100051.
2 J. T. Devreese, in *Encyclopedia of Applied Physics*, ed. G. L. Trigg, VCH, New York, 1996, vol. 14, pp. 383–409.
3 M. Reticcioli, U. Diebold, G. Kresse and C. Franchini, in *Handbook of Materials Modeling*, Springer International Publishing, Cham, 2019, pp. 1–39.
4 H. Zhang and N. G. Park, *JPhys Energy*, 2023, **5**, 021001.
5 P. Nandi, S. Shin, H. Park, Y. In, U. Amornkitbamrung, H. J. Jeong, S. J. Kwon and H. Shin, *Sol. RRL*, 2024, **8**, 2400364.
6 C. Battaglia, X. Yin, M. Zheng, I. D. Sharp, T. L. Chen, A. Azcatl, S. Mcdonell, C. Carraro, R. Maboudian, R. M. Wallace and A. Javey, *Nano Lett.*, 2014, **14**, 967–971.
7 X. Wang, E. Zhang, H. Shi, Y. Tao and X. Ren, *Analyst*, 2022, **147**, 1257–1272.
8 X. Zheng, H. Zhong, Z. Wang, J. Li, Y. Hu, H. Li, J. Jia, S. Zhang and F. Ren, *Vacuum*, 2022, **198**, 110884.
9 H. Dizajghorbani Aghdam, S. Moemen Bellah and R. Malekfar, *Spectrochim. Acta, Part A*, 2020, **224**, 117379.
10 L. Yang, Y. Peng, Y. Yang, J. Liu, Z. Li, Y. Ma, Z. Zhang, Y. Wei, S. Li, Z. Huang and N. V. Long, *ACS Appl. Nano Mater.*, 2018, **1**, 4516–4527.
11 Y. Shi, Q. Liu, R. Hong, C. Tao, Q. Wang, H. Lin, Z. Han and D. Zhang, *Spectrochim. Acta, Part A*, 2022, **268**, 120686.
12 T. Vo Huu, H. Le Thi Thu, L. Nguyen Hoang, K. Huynh Thuy Doan, K. N. Duy, T. D. Anh, H. Le Thi Minh, K. N. Huu and H. Le Vu Tuan, *Nanoscale*, 2024, **16**, 22297–22311.
13 R. He, H. Lai, S. Wang, T. Chen, F. Xie, Q. Chen, P. Liu, J. Chen and W. Xie, *Appl. Surf. Sci.*, 2020, **506**, 145116.
14 L. Lan, X. Hou, Y. Gao, X. Fan and T. Qiu, *Nanotechnology*, 2019, **30**, 505204.
15 A. Zhang, Z. Ding, Z. Shen, Z. Yan, K. Han, J. Li, M. Zhang and W. Zhang, *Talanta*, 2025, **292**, 127934.
16 L. Yang, Y. Yang, Y. Ma, S. Li, Y. Wei, Z. Huang and N. V. Long, *Nanomaterials*, 2017, **7**, 398.
17 K. L. Foo, U. Hashim, K. Muhammad and C. H. Voon, *Nanoscale Res. Lett.*, 2014, **9**, 429.
18 E. Arakelova, A. Khachatryan, A. Kteyan, K. Avjyan and S. Grigoryan, *Thin Solid Films*, 2016, **612**, 407–413.
19 W. Lu, Q. Kang, J. Li, X. Xu, D. Yuan, L. Yang, S. Liu, T. Liu, H. Yan, Z. Wu, W. Hu, J. Wang and Y. Zhang, *Small Struct.*, 2024, **5**, 2400559.
20 H. Zhang, P. Zhang, M. Qiu, J. Dong, Y. Zhang and X. W. (David) Lou, *Adv. Mater.*, 2019, **31**, 1804883.

Open Access Article. Published on 07 October 2025. Downloaded on 2/24/2026 2:39:45 PM. This article is licensed under a Creative Commons Attribution-NonCommercial 3.0 Unported Licence.

21 V. Vaiano, G. Iervolino, D. Sannino, L. Rizzo, G. Sarno and A. Farina, *Appl. Catal., B*, 2014, **160–161**, 247–253.
22 S. Xie, K. Lai, C. Gu, T. Jiang, L. Zhou, X. Zheng, X. Shen, J. Han and J. Zhou, *Mater. Today Nano*, 2022, **18**, 100179.
23 S. Xie, D. Chen, C. Gu, T. Jiang, S. Zeng, Y. Y. Wang, Z. Ni, X. Shen and J. Zhou, *ACS Appl. Mater. Interfaces*, 2021, **13**, 33345–33353.
24 C. Zhao, J. Liu, Y. Guo, Y. Pan, X. Hu, G. Weng, J. Tao, J. Jiang, S. Chen, P. Yang and J. Chu, *J. Mater. Sci.: Mater. Electron.*, 2021, **32**, 9106–9114.
25 H. Le Thi Minh, L. Tran Thi, H. Kim Nhat, H. Nguyen Thi Anh, T. Dao Anh, T. Nguyen Huu, K. Nguyen Duy and H. Le Vu Tuan, *J. Mater. Sci.: Mater. Electron.*, 2023, **34**, 357.
26 S. K. Sardana, A. Singh, S. K. Srivastava and D. K. Pandya, *AIP Conf. Proc.*, 2018, **1961**, 030023.
27 N.-F. Shih, B.-R. Chen and P.-C. Yao, *J. Chin. Inst. Eng.*, 2014, **37**, 863–869.
28 F. Meng, Z. Wang, B. Huo, J. Wang, D. Li, W. Hao, W. Ma, J. Qi, P. Cui, Z. Zhu and Y. Wang, *Appl. Surf. Sci.*, 2023, **627**, 156782.
29 R. Jothilakshmi, V. Ramakrishnan, R. Thangavel, J. Kumar, A. Sarua and M. Kuball, *J. Raman Spectrosc.*, 2009, **40**, 556–561.
30 M. C. Huang, T. H. Wang, S. H. Cheng, J. C. Lin, W. H. Lan, C. C. Wu and W. S. Chang, *Nanosci. Nanotechnol. Lett.*, 2014, **6**, 210–215.
31 V. Karpyna, A. Ievtushenko, O. Kolomys, O. Lytvyn, V. Strelchuk, V. Tkach, S. Starik, V. Baturin and O. Karpenko, *Phys. Status Solidi B*, 2020, **257**, 1900788.
32 R. L. d. S. e Silva and A. Franco Jr, *Mater. Sci. Semicond. Process.*, 2020, **119**, 105227.
33 R. Jothilakshmi, V. Ramakrishnan, R. Thangavel, J. Kumar, A. Sarua and M. Kuball, *J. Raman Spectrosc.*, 2009, **40**, 556–561.
34 T. Vo Huu, V. T. Tran Nhat, M. N. Xuan, H. N. Thi Ngoc, L. N. Hoang, T. D. Anh, K. N. Huu and H. Le Vu Tuan, *RSC Adv.*, 2025, **15**, 14604–14619.
35 W. Zheng, B. Sun, D. Li, S. M. Gali, H. Zhang, S. Fu, L. Di Virgilio, Z. Li, S. Yang, S. Zhou, D. Beljonne, M. Yu, X. Feng, H. I. Wang and M. Bonn, *Nat. Phys.*, 2022, **18**, 544–550.
36 C. Wu, E. Chen and J. Wei, *Colloids Surf., A*, 2016, **506**, 450–456.
37 M. Morales-Luna, S. A. Tomás, M. A. Arvizu, M. Pérez-González and E. Campos-Gonzalez, *J. Alloys Compd.*, 2017, **722**, 938–945.
38 S. Bai, S. Chen, L. Chen, K. Zhang, R. Luo, D. Li and C. C. Liu, *Sens. Actuators, B*, 2012, **174**, 51–58.
39 E. Hasabeldaim, O. M. Ntwaeaborwa, R. E. Kroon and H. C. Swart, *J. Mol. Struct.*, 2019, **1192**, 105–114.
40 A. Sreedhar, J. H. Kwon, J. Yi and J. S. Gwag, *Ceram. Int.*, 2016, **42**, 14456–14462.
41 K. Bandopadhyay and J. Mitra, *RSC Adv.*, 2015, **5**, 23540–23547.
42 A. M. Ramesh and S. Shivanna, *J. Environ. Chem. Eng.*, 2021, **9**, 105040.
43 D. Maity, K. Karmakar and K. Mandal, *J. Alloys Compd.*, 2019, **791**, 739–746.
44 L. J. Li, H. Deng, L. P. Dai, J. J. Chen, Q. L. Yuan and Y. Li, *Mater. Res. Bull.*, 2008, **43**, 1456–1462.
45 M. Dieterle, G. Weinberg and G. Mestl, *Phys. Chem. Chem. Phys.*, 2002, **4**, 812–821.
46 M. T. Greiner, L. Chai, M. G. Helander, W. M. Tang and Z. H. Lu, *Adv. Funct. Mater.*, 2013, **23**, 215–226.
47 H. Le Thi Minh, L. Tran Thi, H. Kim Nhat, H. Nguyen Thi Anh, T. Dao Anh, T. Nguyen Huu, K. Nguyen Duy and H. Le Vu Tuan, *J. Mater. Sci.: Mater. Electron.*, 2023, **34**, 283.
48 Y. Natanzon, A. Azulay and Y. Amouyal, *Isr. J. Chem.*, 2020, **60**, 219–227.
49 D. Scirè, R. Macaluso, M. Mosca, S. Mirabella, A. Gulino, O. Isabella, M. Zeman and I. Crupi, *Solid-State Electron.*, 2021, **186**, 108135.
50 J. Ederth, A. Hoel, G. A. Niklasson and C. G. Granqvist, *J. Appl. Phys.*, 2004, **96**, 5722–5726.
51 Y. Natanzon, A. Azulay and Y. Amouyal, *Isr. J. Chem.*, 2020, **60**, 219–227.
52 E. K. H. Salje, *Philos. Trans. R. Soc., A*, 1994, **347**, 233–242.
53 I. G. Austin and N. F. Mott, *Adv. Phys.*, 1969, **18**, 41–102.
54 A. S. Alexandrov and N. F. Mott, *Rep. Prog. Phys.*, 1994, **57**, 1197–1332.
55 J. R. Lombardi and R. L. Birke, *J. Phys. Chem. C*, 2014, **118**, 11120–11130.
56 J. Ye, R. Arul, M. K. Nieuwoudt, J. Dong, T. Zhang, L. Dai, N. C. Greenham, A. Rao, R. L. Z. Hoye, W. Gao and M. C. Simpson, *J. Phys. Chem. Lett.*, 2023, **14**, 4607–4616.
57 P. Ji, Z. Mao, Z. Wang, X. Xue, Y. Zhang, J. Lv and X. Shi, *Nanomaterials*, 2019, **9**, 983.

© 2025 The Author(s). Published by the Royal Society of Chemistry